Evidence for interatomic Coulombic decay in Xe K-shell-vacancy decay of XeF_2

R. W. Dunford,[1] S. H. Southworth,[1] D. Ray,[1] E. P. Kanter,[1] B. Krässig,[1] L. Young,[1] D. A. Arms,[1] E. M. Dufresne,[1] D. A. Walko,[1] O. Vendrell,[2] S.-K. Son,[2] and R. Santra[2,3]

[1]*Argonne National Laboratory, 9700 South Cass Avenue, Lemont, Illinois 60439, USA*
[2]*Center for Free-Electron Laser Science, DESY, 22607 Hamburg, Germany*
[3]*Department of Physics, University of Hamburg, 20355 Hamburg, Germany*

(Received 26 March 2012; published 4 September 2012)

Charge production, charge redistribution, and ion fragmentation are explored in the decay of a Xe K-shell vacancy in XeF_2. Coincidence measurements of all ionic fragments in XeF_2 provide evidence that an interatomic-Coulombic-decay-like (ICD-like) process plays a role in the cascade decay. The signature of the ICD-like process is an enhancement of the total number of electrons ejected as compared to the case of atomic Xe. The results indicate that the F atoms participate in the decay cascade within the first few femtoseconds after core-hole formation and that fragmentation begins during the decay process.

DOI: 10.1103/PhysRevA.86.033401 PACS number(s): 33.80.Eh, 36.40.−c

I. INTRODUCTION

The photoionization of a deep inner-shell electron in a heavy atom sets off a cascade of radiative and nonradiative transitions as the atom relaxes and leads to a range of final charge states. If the cascade occurs in an atom that is part of a molecule or cluster, it can also lead to the removal of valence electrons on more than one atomic site and produce two or more charge centers, which is followed by a Coulomb explosion of the system [1,2]. The molecular damage triggered by such events can potentially be used in new radiotherapy techniques based on the insertion of iodinated compounds into tumorous regions, which are then exposed to synchrotron radiation above the K edge of the heavy atom [3]. An understanding of decay processes in electronically excited molecules is also particularly important in plasma physics and astrophysics and can be an important source of low-energy electrons and energetic reactive ions [4,5] that produce radiation damage in biological systems [6–8].

The common hypothesis for deep inner-shell decay in a molecular environment is that of a localized cascade decay on the heavy atom accompanied by charge redistribution and Coulomb explosion [1,2,9,10]. Within this scenario, the same total final charge is produced in the cascade decay of an isolated heavy atom and in the decay of the same atom embedded in an environment. Here we explore the total charge production after deep inner-shell ionization of a heavy atomic species and find an enhanced total charge production if the heavy atom is bound in a molecule. Specifically, we have carried out both experimental and theoretical investigations of the relaxation mechanisms of atomic Xe and of molecular XeF_2 following Xe K-shell photoionization. XeF_2 constitutes a model system for the ionization and fragmentation of iodinated compounds. Our results indicate that the F atoms participate in the decay cascade and enhance the total charge production, and that fragmentation of the molecule begins already during the decay process. We attribute the observed enhancement in total charge production to interatomic-Coulombic-decay-like (ICD-like) processes during the cascade decay. Such processes involve decay channels exclusively open due to the presence of neighboring atoms [11–19]. Therefore, this mechanism results in the production of higher charge states in a molecular environment than would be expected from an isolated atom. We note that other molecular effects such as charge migration or enhanced Auger rates due to an environment could also contribute to these effects, but they are not able to explain the observed enhanced charge production. In classical ICD examples, a single inner-valence-shell vacancy in an atom or molecule decays *only* in the presence of a neighbor into two outer-valence vacancies, one in each subsystem, thus enhancing the total final charge.

II. EXPERIMENT

Our choice of Xe and XeF_2 was motivated by the fact that both systems may be studied in the gas phase, thus making it possible to resolve the fragmentation channels and energies of the fragments in a way that would not be possible in a condensed-phase experiment. The instruments were similar to those used in Ref. [20] and consisted of an energy-dispersive high-purity-Ge x-ray fluorescence spectrometer and an ion time-of-flight (ITOF) spectrometer. Measurements were made at beamline 7ID at Argonne's Advanced Photon Source (APS) with an undulator and double-crystal monochromator [21]. To produce an intense, narrowband x-ray beam that could be tuned across the Xe K edge at 34.5 keV [22], the fifth-order harmonic of the undulator radiation was used, and the monochromator was operated with diamond (333) reflections. This produced a narrow energy spread estimated to be <1 eV, which is much less than the K-hole lifetime width $\Gamma(K) = 11.49$ eV [23]. The x-ray beam was crossed with effusive beams of Xe or XeF_2. The samples flowed into the interaction region through a stainless-steel capillary tube. The XeF_2 vapor originated from a solid sample at room temperature, and the flow was controlled with a needle valve. The x-ray fluorescence and ITOF spectra were recorded in coincidence with an event-mode (list-mode) data acquisition system.

In order to start with a well-defined initial state, we selected only those events in which the first step in the decay of the Xe K-shell vacancies was via x-ray fluorescence, the strongest decay mode. This was done by detecting the Xe K x rays using a low-energy photon spectrometer (LEPS) located on one side of the interaction region (see Fig. 1). This spectrometer was

 ©2012 American Physical Society

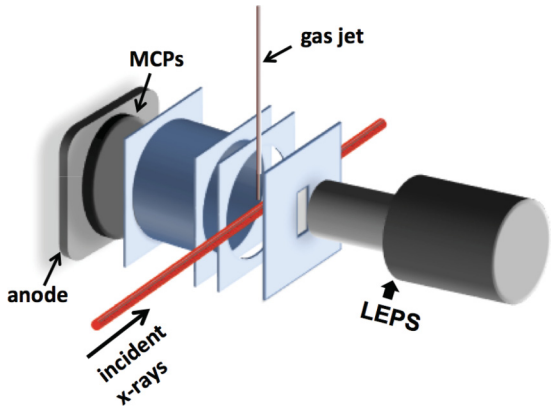

FIG. 1. (Color online) Schematic of the apparatus in the target area. A Ge x-ray fluorescence spectrometer (LEPS) on one side of the interaction region measures x rays from the target. An ion time-of-flight (ITOF) spectrometer on the opposite side is used to measure the charge-to-mass ratios of the ion fragments produced. The x-ray beam from the Advanced Photon Source was crossed with effusive beams of Xe or XeF_2. The x-ray beam is linearly polarized along the spectrometer axis.

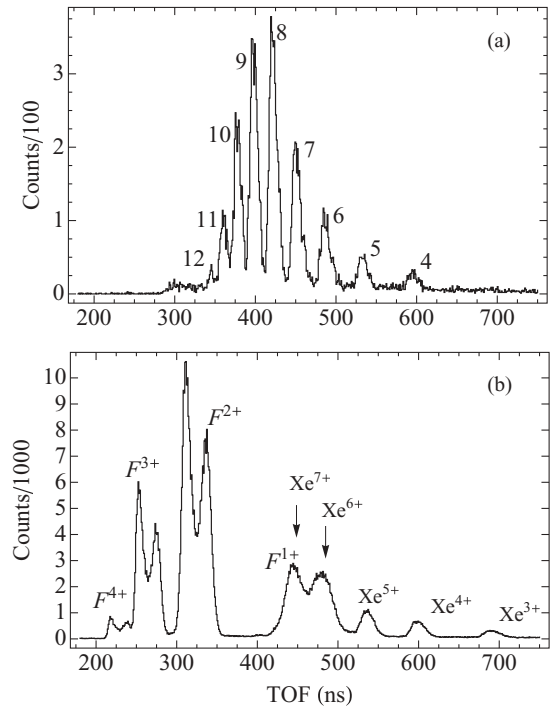

FIG. 2. Ion time-of-flight spectra for all ions recorded in coincidence with a $K\alpha$ photon. (a) K-shell-ionized Xe. Peaks due to Xe^{q+} are labeled by the charge state q. (1 h accumulation.) (b) XeF_2 excited at the $1s^{-1}7\sigma_u$ molecular resonance. Ions of charge q are labeled F^{q+} and Xe^{q+}. (6 h accumulation). The asymmetric splitting of the F^{q+} peaks is explained in the text. The XeF_2 data show F^{q+} charge states from +1 to +4 and Xe^{q+} ions from +3 to +5. Less obvious are contributions from Xe^{6+} and Xe^{7+} which overlap the F^{1+} peak.

able to resolve the $K\alpha$ and $K\beta$ fluorescence lines, so it also provided a tag for the first step in the cascade. Note that a $2p$ (4893 eV) or $3p$ (961 eV) hole remains highly localized on the Xe atom of XeF_2.

The detected photons provide the start signal for the ITOF spectrometer. Following formation, the ions were accelerated and detected using a Z-stack microchannel-plate detector (MCP). The MCP was connected to a multihit time-to-digital converter. One difficulty with this scheme is that the slow rise time of the LEPS signals leads to an unacceptable spread in start times. We circumvented this problem by using the excellent timing available from the synchrotron bunch structure. The 80 ps wide bunches are separated by 153 ns and the Ge timing resolution (about 50 ns) is good enough to identify the particular bunch associated with the event, so we were able to correct the fluorescence start times using the synchrotron timing signals. In this way, we obtained sharp ITOF peaks. More details on this procedure are given in Ref. [20]. The ion acceleration was accomplished using an extraction field of 1575 V/cm toward the MCP, which was biased at −4 kV.

Ion TOF spectra were taken alternately for targets of Xe and XeF_2. For each event of the XeF_2 data, the multihit ion detector recorded one, two, or three atomic ions but no molecular ions. Typical spectra for all ions detected in coincidence with detection of a Xe $K\alpha$ photon are presented in Fig. 2. The ion spectra show immediately that charge on the Xe atom [Fig. 2(a)] is redistributed to the F ligands [Fig. 2(b)]. Typical rates for XeF_2 data were 60 Hz for the x-ray spectrometer and 2 kHz for the ion detector. The APS storage ring generated x-ray pulses at a frequency of 6.5 MHz, so the probability for two photoionization events occurring in the same beam pulse was negligible.

For the XeF_2 data in Fig. 2(b), the beamline monochromator was set near a preedge resonance attributed to excitation of a Xe $1s$ electron to the lowest unoccupied molecular orbital, i.e., the antibonding $7\sigma_u$ virtual orbital identified in Hartree-Fock self-consistent-field calculations [24]. Resonant photoabsorption preferentially excited molecules whose internuclear axes were aligned with the x-ray polarization direction, and the axis of the ITOF spectrometer was also positioned along this direction. The (on-resonance) fluorine ion peaks show distinct splittings into faster and slower components corresponding to ions ejected toward and away from the detector in the fragmentation process. This separation between the backward- and forward-going ions provided a means to extract information on the breakup modes, and for this reason, the experiment is based on the data obtained using resonance excitation. The asymmetries in the intensities of the faster and slower F ion components in Fig. 2(b) are due to instrumental effects such as dead time, as explained in Appendix D.

The multiple-hit ITOF spectrometer allows us to look at second and third hits and so we can potentially record all three ion fragments of XeF_2. In particular, it is interesting to look at a scatter plot of the correlation between the first and second hits. This is shown in Fig. 3, which shows data taken with the monochromator set to the $1s^{-1}7\sigma_u$ resonance. The first-hit ITOF is plotted along the vertical axis and the second-hit ITOF is plotted along the horizontal axis. The four horizontal stripes correspond to fluorine ions with charge states (from top to bottom) 1+ to 4+. The less prominent vertical stripes are due to F and Xe ions which are detected in the

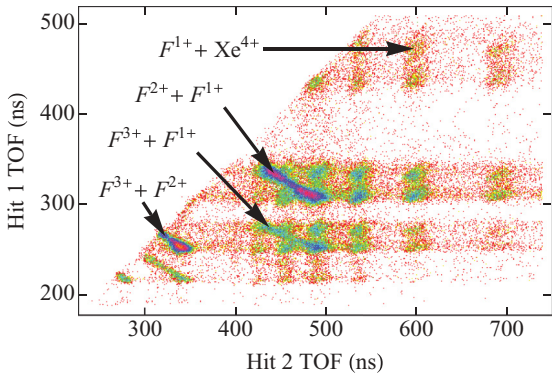

FIG. 3. (Color online) Scatter plot of hit 1 vs hit 2 for XeF_2 fragmentation events in coincidence with a $K\alpha$ photon. The incident x-ray energy was set to the $1s^{-1}7\sigma_u$ resonance.

second hit. Most of the intensity in the plot is concentrated at the intersections of these stripes. Both the first and second hits show the lobe structure for each F charge state. Note the coincidences between F^{2+} ions detected in the first hit and F^{1+} ions detected in the second hit. We see that the "fast" lobe of the F^{1+} peak correlates with the "slow" lobe of the F^{2+} peak, and vice versa. The dominance of these events gives confidence that there is only one molecular ionization per event, since otherwise the correlation would be washed out. These correlations are also consistent with the picture that, in the molecular breakup, one of the fluorine ions has initial momentum toward the MCP detector and the other has initial momentum away from it.

To analyze the second-hit ion data correlated with the first-hit ion data, it is useful to project *each* lobe of the first-hit F ion charge states onto the hit-2 axis. This gives a hit-2 spectrum for each of the lobes. At the same time, we extract more information from some of the blended lines. To see the idea, consider Fig. 4, which shows the two spectra obtained by projection of the two lobes of the hit-1 F^{2+} charge state onto the hit-2 axis. It is difficult to obtain any information about the Xe^{7+} charge state from the upper spectrum, Fig. 4(a), since the more intense F^{1+} peak lies on top of it, but the situation in Fig. 4(b) is better. There is a significant bulge on the left side of the F^{1+} line and this is readily fitted to two peaks (F^{1+} and Xe^{7+}), revealing the Xe^{7+} count. By examining the ratios between the clearly resolved Xe^{5+} and Xe^{4+} peaks in the upper and lower spectra, we can make a reasonable estimate about the expected strength of the Xe^{7+} peak in the upper spectrum [Fig. 4(a)] based on the fit to Fig. 4(b). Similar considerations can be used to get better information for the (F^{2+},Xe^{6+}) combination.

The aim of the analysis of the XeF_2 data was to determine the probabilities for each of the possible charge-distribution channels (Xe^{q_1+},F^{q_2+},F^{q_3+}) in coincidence with detection of a Xe $K\alpha$ x ray. We developed a model of the experiment with parameters determined by best fitting to the data. The details are presented in Appendix B. The analysis provided probabilities of all of the possible breakup modes. The results for the various fluorine breakup patterns (F^{q_2+},F^{q_3+}) summed over all Xe^{q_1+} partners are given in Table I. This shows that ~70% of the molecular ions break up with equally charged F

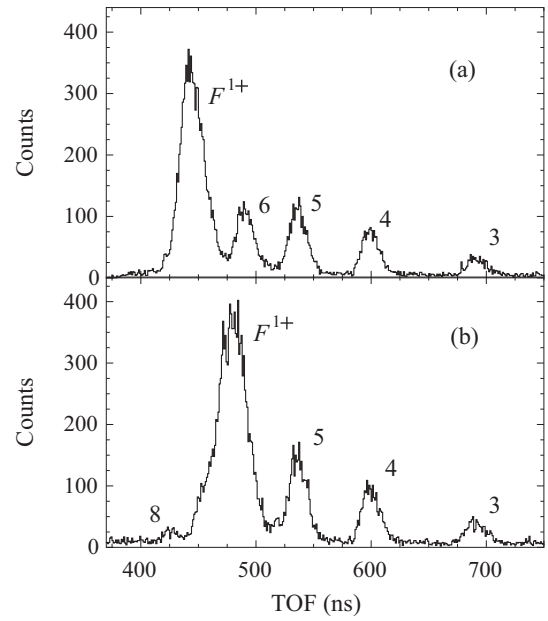

FIG. 4. Projections from the hit 1 vs hit 2 scatter plot. (a) Projection of the slow component of the F^{2+} peak onto the hit-2 axis. (b) Projection of the fast component of the F^{2+} peak onto the hit-2 axis.

ions. The complete table of charge-distribution probabilities is provided in Table IV.

Some results from the XeF_2 breakup probabilities in coincidence with a $K\alpha$ photon are compared with the atomic Xe charge distributions in Fig. 5. In Fig. 5(a) we show the breakup pattern for the subset of events involving (F^{3+},F^{2+}) coincidences, showing the fraction of events in this subset with a given total charge, and compare it to the charge-state distribution for the atomic Xe target under similar conditions. These data are based on observation of triple ion coincidences (actually fourfold coincidences including the $K\alpha$ photon) and are not dependent on our fit to a model of the experiment. This figure shows a significant shift in the total charge produced following photoionization of XeF_2 compared to the atomic Xe case, indicating that some breakup modes produce more

TABLE I. Experimentally deduced charge distributions for Xe K-shell-vacancy decay of XeF_2 in coincidence with $K\alpha$ fluorescence. The probabilities are given for (F^{q_2+},F^{q_3+}) breakup modes summed over all Xe^{q_1+} partners.

Breakup mode	Probability(error)
(F^{1+},F^{1+})	0.231(20)
(F^{2+},F^{1+})	0.129(31)
(F^{2+},F^{2+})	0.385(44)
(F^{3+},F^{1+})	0.061(14)
(F^{3+},F^{2+})	0.098(6)
(F^{3+},F^{3+})	0.075(16)
(F^{4+},F^{1+})	0.004(3)
(F^{4+},F^{2+})	0.011(5)
(F^{4+},F^{3+})	0.002(1)
(F^{4+},F^{4+})	0.005(2)

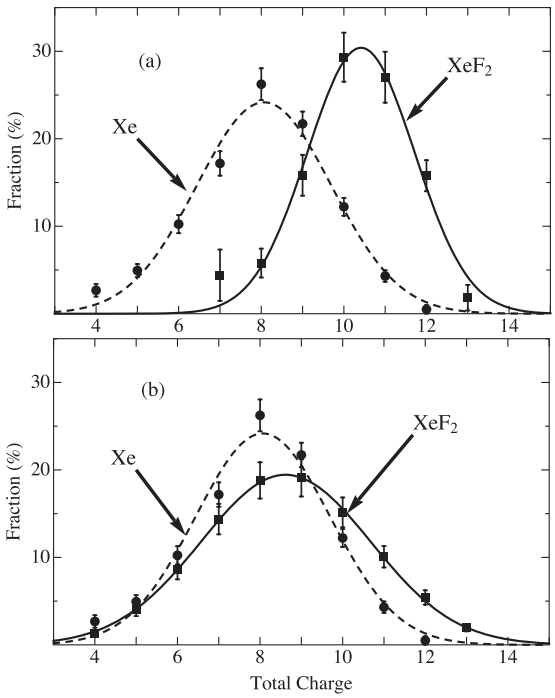

FIG. 5. Charge-state distributions for XeF_2 (squares with solid curve) compared with Xe (circles with dashed curve) in coincidence with $K\alpha$ photons. (a) XeF_2 breakup pattern for the subset of events involving two fluorine ions in the final state with charge states F^{3+} and F^{2+}. We plot the fraction of events (in %) vs the total charge (i.e., the Xe charge state plus 5). (b) The distribution of total charge averaged over all XeF_2 breakup modes.

charge than the atomic Xe case. In Fig. 5(b), the distribution of the total charge of all three ions, summed over all XeF_2 breakup modes, is compared with the charge-state distribution for atomic Xe. The mean value of the charge-state distribution increases from +8.1 in atomic Xe to +8.6 in molecular XeF_2; the total charges of +11 and +12 have significantly higher probabilities in comparison to the atomic case. Nonresonant photoionization, in contrast to excitation of a K-shell electron into the lowest unoccupied molecular orbital, would lead to an even larger charge enhancement. Note that an increment or decrement of decay rates will by itself not change the final charge production. Also charge migration within the molecule does not affect the total charge state. Therefore, the fact that XeF_2 reaches higher charge states than Xe does is evidence that ICD-type channels exist in a deep inner-shell-decay cascade. Besides ICD, direct impact ionization by Auger electrons from Xe can lead to a charge enhancement by knockout of another electron from the two F atoms. We estimate, based on electron impact ionization cross sections, that the charge enhancement due to direct impact ionization is at most +0.1 and therefore cannot account for our experimental observation.

The F^{q+} breakup kinetic energies can be determined from the time-of-flight splittings between the faster and slower components in Fig. 2(b) under the assumption of symmetric F^{q+} partner ions. These energies are compared in Table II with the Coulomb repulsion energies the ions would have if they were formed instantaneously at the ground-state Xe-F internuclear separation of 1.97 Å. The Coulomb energies were calculated by averaging over all possible Xe and F partner ions weighted by charge-distribution probabilities and detection efficiencies. Results are also given for averaging over only the symmetric breakup modes. In either case, the measured energies are lower than the Coulomb energies, which suggests that the ions begin moving away from their ground-state positions before their charges are fully developed.

TABLE II. Kinetic energies (eV) of F^{q+} ions from fragmentation of XeF_2 compared with Coulomb energies calculated at the ground-state Xe-F internuclear distance 1.97 Å. Coulomb energies are averaged over F and Xe partner ions weighted by charge-distribution probabilities and ion detection efficiencies. Results for symmetric breakup modes are listed in column 3 and for all breakup modes in column 4.

F^{q+}	Experiment	Symmetric modes	All modes
F^{1+}	27 ± 1	36	43
F^{2+}	58 ± 1	78	77
F^{3+}	93 ± 2	137	116
F^{4+}	126 ± 7	218	157

III. THEORY

The decay cascade for atomic Xe after K-shell ionization was simulated with the XATOM code [25]. The calculation involves Auger and Coster-Kronig rates, fluorescence rates, and shake-off branching ratios after K-shell ionization, based on the Hartree-Fock-Slater (HFS) method. We analyzed the appearance of vacancies in the $5p$ shell as a function of time, and the results are presented in Fig. 6. The Xe $5p$ shell will be mostly involved in forming molecular orbitals in combination with the outer valence orbitals of F in XeF_2 [24]. Therefore, the dynamics of the $5p$ electrons in Xe is used as a model to estimate the time scale for which the cascade in XeF_2 would start to involve molecular orbitals and for which ionization in the F atoms should be expected. Although the atomic model is not capable of directly reproducing the total charge enhancement seen in the experiment, it provides nonetheless a valid means of estimating time scales for the hole dynamics in the molecule. The number of inner-valence and core holes in Xe reaches its final value after about 2 fs. Subsequently, holes are produced in the outer valence shell, and therefore

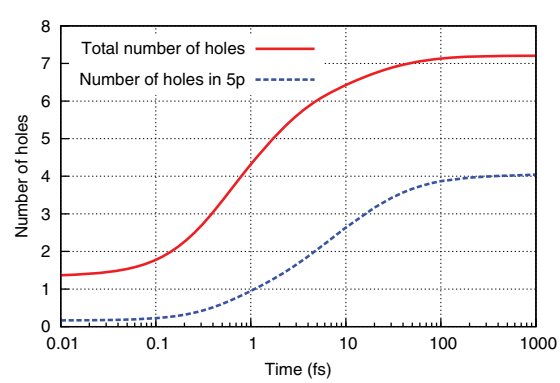

FIG. 6. (Color online) Time evolution of the total number of holes and the population of $5p$ holes in the decay of a Xe K-shell vacancy.

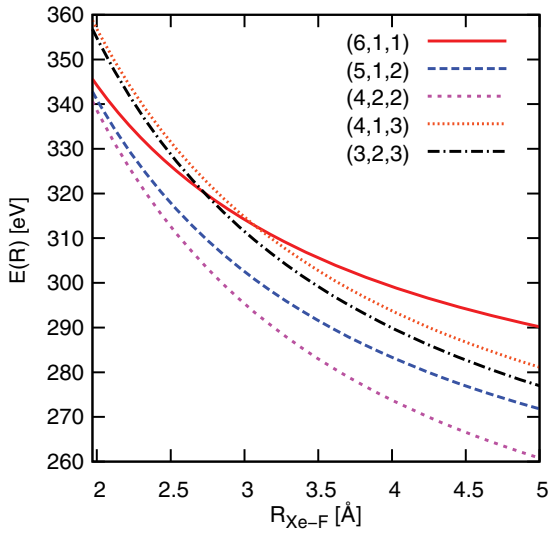

FIG. 7. (Color online) Fragmentation potentials of a XeF_2 ion complex calculated with the independent-ion model for total charge 8+. The numbers in parentheses correspond to (q_1,q_2,q_3). Both Xe-F bonds are elongated symmetrically.

are assumed to correspond to F holes in XeF_2. Following this argument, the Xe atom becomes charged by an average of +4 to +5 during the first 2 fs. The valence holes appear later, and in the first 10 fs two such holes are produced on average.

The time scale of the decay cascade discussed above explains the difference between the experimentally measured kinetic energies of the F fragments in Table II and the values estimated for a Coulomb explosion from the equilibrium geometry. Taking as an example the F^{2+} case, the (4,2,2) channel would yield F ions with a kinetic energy of 64 eV for a Coulomb explosion from the ground-state equilibrium geometry. By considering that the explosion takes place in a (4,1,1) charge distribution during the first 10 fs, and after that the final (4,2,2) distribution is reached, the final kinetic energy is lowered to about 58 eV, already in the range of the experimentally observed values.

Within a given total charge mode, certain fragmentation channels are more preferred than others. To investigate this, potential energy surfaces (PESs) for each fragmentation channel were calculated based on an independent-ion model. For a system of N ions, the energy is given by

$$E^C_{q_1,\ldots,q_N}(\vec{R}_1,\ldots,\vec{R}_N) = \sum_{i=1}^{N} I^{(i)}_{q_i} + \sum_{i>j}^{N} \frac{q_i\, q_j}{|\vec{R}_i - \vec{R}_j|}, \qquad (1)$$

where $\vec{R}_i$ and q_i are the position and charge of the ith ion, respectively, and C is the total charge. $I^{(i)}_{q_i}$ refers to the q_ith ionization potential of the ith atom in its ground electronic state. The ionization potentials $I^{(i)}_{q_i}$ used here were computed at the HFS level for each ion using XATOM. The last term corresponds to the Coulomb repulsion between the ions.

As previously indicated, about 70% of the fragmentation occurs through symmetric charge distributions of the F atoms, mostly involving the (F^{1+},F^{1+}) and (F^{2+},F^{2+}) channels. Moreover, the breakup probabilities show that, for every total final charge, only a reduced subset of the possible fragmentation channels becomes appreciably populated. The subset of populated fragmentation channels within a particular total charge belongs in all cases to the group of channels with the lowest PES as computed with the independent-ion model. These channels minimize the sum of ionization potentials and Coulomb repulsion for distances of the ions within about 1 Å of the ground-state equilibrium distance. For example, the (6,1,1) channel shown in Fig. 7 is about seven times more populated than (3,2,3) (Appendix B).

IV. SUMMARY

Summarizing, the molecular environment leads to an enhanced total charge production in XeF_2 after K-shell ionization of Xe. Using an atomic model, we calculate time scales for various stages of the cascade and find that nuclear dynamics must start to play a role before the cascade is over. This is consistent with measured kinetic energies of the ions. We provide evidence of ICD in this regime by comparing the atomic charge distribution with the molecular total charge distribution obtained by coincidence measurement of all ions originating from the parent molecule. XeF_2 can be regarded as a model for iodinated compounds. In those, a larger number of neighboring atoms in more extended environments could lead to even more pronounced effects than reported here.

ACKNOWLEDGMENTS

We are grateful to K. Lister and I. Ahmad for help with the x-ray fluorescence spectrometer. This work was supported by the Chemical Sciences, Geosciences, and Biosciences Division and the Advanced Photon Source by the Office of Basic Energy Sciences, Office of Science, US Department of Energy, under Contract No. DE-AC02-06CH11357.

APPENDIX A: DETECTION EFFICIENCY AND SYSTEMATIC EFFECTS

In order to determine the charge-state distributions arising from photoionization of Xe and XeF_2, we need the detection efficiencies for the various Xe and F ions in our ITOF apparatus. For the F ions we could not make an independent determination of the detection efficiencies, so these were treated as unknowns in the analysis of the XeF_2 data, as discussed in the next section. For the case of Xe ions, however, we were able to make an independent determination. The method for doing this is based on coincidences between $K\alpha$ x rays and ITOF signals. For our experimental conditions, to good approximation, only one Xe ion at a time is present in the ITOF spectrometer. Assuming this, we define the following quantities for the case of the atomic Xe target:

$N_{K\alpha}$ is the number of $K\alpha$ photons detected in a counting period;

$n^d_{K\alpha}(i)$ is the number of Xe ions of charge state i detected in coincidence with a $K\alpha$ photon during a counting period;

$f_{K\alpha}(i)$ is the fraction of ions in an event that result in a final charge state i following emission of a $K\alpha$ x ray;

$\epsilon(i)$ is the total probability of detecting a Xe ion of charge state i formed in the interaction region; and

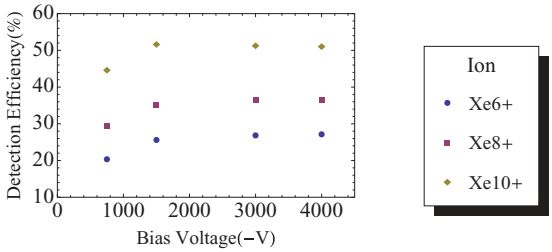

FIG. 8. (Color online) Detection efficiency vs the bias on the MCP for selected charge states.

$c_{Ka}(i)$ is the probability that a coincidence is recorded assuming a $K\alpha$ x ray and a Xe^{i+} ion are both detected in an event.

Using this notation the following relation holds for $n^d_{K\alpha}(i)$:

$$n^d_{K\alpha}(i) = N_{K\alpha} f_{K\alpha}(i)\epsilon(i)c_{Ka}(i). \tag{A1}$$

Of most interest is the total efficiency for detecting a Xe ion of charge state i for an event in which a $K\alpha$ x ray has been detected. We define this to be

$$\epsilon_{K\alpha}(i) \equiv \epsilon(i)c_{Ka}(i). \tag{A2}$$

Solving for the total coincidence efficiency we have

$$\epsilon_{K\alpha}(i) = n^d_{K\alpha}(i)/N_{K\alpha} f_{K\alpha}(i). \tag{A3}$$

The parameter $n^d_{K\alpha}(i)$ is determined by fitting the Xe charge-state distribution for events in coincidence with a $K\alpha$ x ray for a particular counting period. For $f_{K\alpha}(i)$ we used the theoretical Xe charge-state distribution for a weighted average of initial L_2 and L_3 holes calculated by Kochur *et al.* [26]. The calculations agree well with the measured distributions from Ref. [27]. As an aid in determining the optimum experimental parameters, we studied the Xe ion efficiency as a function of the settings on the ITOF spectrometer and explored various nozzle backing pressures.

To study the dependence of the efficiency on the ITOF voltages, we took a series of spectra for different sets of voltages on the spectrometer plates and grids. Each spectrum was fitted to a series of Gaussian peak profiles and the area under each peak gives the count $n^d_{K\alpha}(i)$. We also determined the parameter $N_{K\alpha}$ for each spectrum. Then, using Eq. (A3), the Xe detection efficiencies were determined for each set of voltages. In Fig. 8 we show the dependence of the detection efficiency on MCP bias for several Xe charge states. There is a general rise in detection efficiency with bias voltages with a plateau beginning about 3000 V. Based on these preliminary studies, we chose the final voltages for the TOF spectrometer. We also studied the effect of background pressure on the ITOF spectra. The efficiencies for detecting Xe ions were determined at low enough background pressure that the pressure-related errors were relatively small compared to the overall errors in determining the detection efficiencies. For the XeF_2 data, higher pressures had to be used. We studied the effect of these higher pressures using the atomic Xe target since we had better control with that target. The results could not be directly applied to correct the XeF_2 data. Instead, based on this study, we increased the uncertainties in the measured XeF_2 charge-state distributions by 5%.

APPENDIX B: DATA ANALYSIS TO DETERMINE THE XeF_2 BREAKUP MODES

Here we describe our method to determine the charge distribution channels (CDCs) for the XeF_2 data in coincidence with detection of a Xe $K\alpha$ x ray and with the monochromator set to the $1s^{-1}7\sigma_u$ resonance. In an ideal experiment, one would have independent determinations of the detection efficiencies of all of the Xe and F ion charge states and triple-coincidence data for each CDC. It would then be a straightforward matter to obtain the experimentally observed probability for each CDC. As discussed above, although we have an independent measurement of the detection efficiency for the Xe ions, this is not the case for the F ions. Also, since we were not able to record separate hits for ions arriving at the MCP at nearly the same time ($\Delta T < 50$ ns), triple-ion-coincidence data are missing for many CDCs. Nevertheless, we were able to obtain information on all CDCs by combining results from the different data types: single ion hits, binary ion coincidences, and triple ion coincidences. We developed a model of the experiment with parameters determined by best fitting the three different types of data. The analysis provided probabilities of all of the possible breakup modes and also determined the detection efficiencies for the F ions. The analysis depended on the use of resonance excitation which provided a clear separation between forward and backward ions. The additional relations provided by these two classes of F ions were required to solve for the unknowns in the problem.

The three classes of spectra used to determine the XeF_2 CDC are (1) the first-hit spectrum; (2) second-hit data with a condition that the first hit was from a specific F^{q+} peak, with separate projections for the "fast" and "slow" lobes; (3) hit-3 spectra (Xe) for each combination of hit-1 and hit-2 fluorine ion charge states (F^{q+},$F^{q'+}$) for which data exist (in this case the "fast" and "slow" modes are combined).

The first-hit spectrum was fitted to eight fluorine peaks (two per charge state) and the Xe^{q+} peaks appearing in this spectrum. There are eight members of the second class of spectra, one from each of the eight fluorine hit-1 lobes. Fits are done to each of these spectra to determine all the fluorine and xenon ion peaks. Five combinations of fluorine charge states from (hit-1,hit-2) provided spectra of the third class. These are [(F^{3+},F^{2+}), (F^{4+},F^{2+}), (F^{2+},F^{1+}), (F^{3+},F^{1+}), and (F^{4+},F^{1+})]. These spectra were each fitted to determine the Xe ion distributions in each case. Taking the three classes of spectra together gives a total of 14 spectra to analyze for this run.

The first step is to determine the probabilities for the charge-state breakup patterns of the two fluorine ions, and to this end we define the following parameters:

$r_{a'}[i]$: the count in each of the eight fluorine peaks (two for each charge state) in the first-hit spectrum, divided by the total number of $K\alpha$ photons detected. These data are obtained by fitting the XeF_2 first-hit spectrum for eight fluorine peaks.

$r_{a'}[0]$: the number of $K\alpha$ photons less the number of F atoms detected in the first hit.

$r_{2a'}[i,j]$: the number of coincidences between fluorine ions in which the faster ion (hit 1) has index i and the slower ion (hit 2) has index j. Each index runs through the eight fluorine peaks.

$f_{a'}[i,j]$: the fraction of XeF_2 molecules for which there are two fluorine ions in the breakup pattern with the faster fluorine ion having label i and the slower fluorine ion having label j.

$f_{a'}[i,0]$: the fraction of XeF_2 molecules that break up with only one charged fluorine ion with index i.

$f_{a'}[0,0]$: the fraction of XeF_2 molecules that break up with two neutral fluorine atoms.

$\epsilon'_F[i]$: the total detection efficiency for the fluorine ion with index i. Initially we assume a different detection efficiency for ions going toward or away from the detector, so the index runs through the eight fluorine peaks.

Then we write down eight relations for the measured quantities $r_{a'}[k]$ giving the number of events per detected $K\alpha$ photon in which a fluorine ion labeled with index k was detected:

$$r_{a'}[k] = \epsilon'_F[k]\left(f_{a'}[k,0] + \sum_l f_{a'}[k,l] + \sum_l (1-\epsilon'_F[l]) f_{a'}[l,k]\right). \tag{B1}$$

The sums over l include all physically realizable combinations. In particular, according to the above definitions, the first index in $f_{a'}[i,j]$ labels the ion with the shorter time of flight, which eliminates many possible terms from the sums. The first term inside the parentheses gives the fraction of events in which only one charged fluorine ion was produced and this was of the species labeled k. The second term gives the fraction of events in which two charged fluorine ions were produced and the ion of index k is the faster (has a shorter ITOF) of the two fluorine ions, while the last term gives the fraction of events in which the ion with index k was the slower of the two, but it was possible that it could have been detected in the first hit, because the faster fluorine ion (labeled l) was not detected. All three of the terms in the large parentheses are multiplied by $\epsilon'_F[k]$, the probability of detecting an ion labeled with index k. In writing Eq. (B1), we make the simplification of neglecting a small number of cases in which a Xe ion with charge greater than +5 is detected in the first hit thus "blocking" detection of a F^{1+}. We increase the error in the detection efficiency to account for this.

We also get a relation for $r_{a'}[0]$, the fraction of events in which a $K\alpha$ photon was detected but no fluorine ion was detected:

$$r_{a'}[0] = f_{a'}[0,0] + \sum_l (1-\epsilon'_F[l]) f_{a'}[l,0] + \sum_{l,k} (1-\epsilon'_F[l])(1-\epsilon'_F[k]) f_{a'}[l,k]. \tag{B2}$$

The first term is the fraction of events for which no charged fluorine ions are produced. The second term is the fraction of events where one fluorine ion l was formed but was not detected. The third term is the fraction of events where two fluorine ions were produced but neither was detected.

For the second hit, coincidences between F ions were determined from the count in each two-dimensional peak. Again neglecting "blocking" from faster Xe ions, we can write the following expression:

$$r_{2a'}[i,j] = \epsilon'_F[i]\epsilon'_F[j] f_{a'}[i,j]. \tag{B3}$$

We have data for only ten of the $r_{2a'}[i,j]$. Although there are eight values for each index, many possible combinations (i,j) of indices are nonphysical or correspond to cases in which we have no data. For example, if both F ions have the same charge, their times of flight cannot be separately resolved; also, since we are working at the $1s^{-1}7\sigma_u$ molecular resonance, one of the indices labels a fluorine ion moving toward the MCP so the other index is restricted to values corresponding to an ion which initially moves away from the MCP.

Finally, we have the relation that the sum over all of the $f_{a'}[i,j]$ is equal to 1 (generalizing the sum to include cases involving neutrals, i.e., $f_{a'}[i,0]$ and $f_{a'}[0,0]$). Counting this relation, together with Eqs. (B1)–(B3), we have 20 equations relating the measured quantities to the eight fluorine detection efficiencies $\epsilon'_F[i]$ and 25 physically realizable fluorine breakup modes $f_{a'}[i,j]$, i.e., 33 unknowns.

Although there are too many unknowns to allow a solution to these equations, we can gain some insight by solving the system after modifying the equations based on various assumptions for the parameters, such as setting some of the obviously small parameters equal to zero, or assuming that the detection efficiency is independent of whether the fluorine starts out going toward or away from the detector, or assuming a functional form for the fluorine detection efficiency. Based on a study of these trial solutions, we chose a set of assumptions that allows us to propose a plausible scenario for the probabilities of the various XeF_2 CDCs following photoionization at the $1s^{-1}7\sigma_u$ resonance in XeF_2. Therefore, to proceed, we make three assumptions:

(1) For each ionic breakup mode (F^{i+},F^{j+}), the number of ions produced with momentum initially toward the MPC is equal to the number of ions with momentum initially away from the MPC.

(2) The detection efficiency does not depend on whether the initial velocity is toward or away from the MCP.

(3) Three charged ions are produced in each event.

The first assumption seems reasonable from symmetry arguments. The second assumption is consistent with the results of some ion trajectory calculations used to model our ITOF spectrometer (see Appendix D). The third assumption is justified by the fact that we do not see any binary XeF^{q+} molecules in our data. Also, with an average Xe^{q+} charge state of Xe^{8+} it is reasonable to assume that valence electrons are pulled from both F atoms.

Taken together, the three assumptions allow the reduction to a new set of equations where the breakup patterns contain four values for each index, instead of eight. When this is done, we obtain 15 independent equations in 14 unknowns, which give an overconstrained system. The solution to the reduced equation set gives ten F ion breakup modes $f_a[i,j]$ (see Table I), and four fluorine ion detection efficiencies $\epsilon_F[i]$ (Table III). Here the primes are removed to indicate that there are only four values for each index for these parameters. Note that the new equations still involve all 20 input data parameters $r_{a'}[i]$, $r_{a'}[0]$, and $r_{2a'}[i,j]$, which use the original eight indices as indicated by the primes. The point is that no data were thrown away in reducing the equations. In particular,

TABLE III. Detection efficiencies $\epsilon_F[i]$ for fluorine ions F^{i+}.

Fluorine ion	Detection efficiency (error)
F^{1+}	0.15(1)
F^{2+}	0.31(1)
F^{3+}	0.46(2)
F^{4+}	0.58(12)

the asymmetry in the two lobes for each charge state is an important feature of the data which must be "explained" by the solution to the new set of equations.

The results indicate that modes with high total fluorine charge are unfavorable. The errors are propagated from the errors assigned to the input parameters $r_{a'}[i]$, $r_{a'}[0]$, and $r_{2a'}[i,j]$ obtained from the data, i.e., they are a combination of statistical and systematic errors.

Hit-3 spectra for events in which we detected fluorine ions in both the first and second hits give Xe charge-state distributions for particular combinations of fluorine ions (after correction for Xe ion detection efficiency). Events in which we have such hit-3 data provide the best information on the XeF_2 distributions for various fluorine breakup modes since the fluorine charge states have been identified for each Xe ion. However, in some cases, the two fluorine ions arrive too close together in time to be separately resolved. In the end, we get six xenon ion TOF spectra by cutting on different combinations of fluorine peaks in the first two hits (this time summing the two lobes of each fluorine peak). The spectra correspond to the fluorine combinations (F^{3+},F^{2+}), (F^{4+},F^{2+}), (F^{4+},F^{3+}), (F^{2+},F^{1+}), (F^{3+},F^{1+}), and (F^{4+},F^{1+}). Fitting each of these spectra, we obtain the count in each Xe ion charge state. These data form a three-dimensional array in which the first two indices refer to the fluorine charge states for the first and second hits and run from 1 to 4. The third index refers to the Xe charge state. At this point we have four unknown Xe distributions, associated with the fluorine combinations (F^{1+},F^{1+}), (F^{2+},F^{2+}), (F^{3+},F^{3+}), and (F^{4+},F^{4+}).

We now ask whether we can get some information on these four unknown Xe ion distributions by studying the Xe ions in the hit-1 and hit-2 spectra. At first glance, it appears that if a F^{q_1} ion is detected in hit 1 and a Xe ion is detected in hit 2, we generally cannot get any information on the other F^{q_2} ion from that event. If a Xe ion is detected in hit 1, then the situation is even worse, since we generally cannot get any information on either fluorine ion in that event.

However, if we try to reconstruct the hit-2 spectra using the six known (F^{q2},F^{q3},Xe^{q1}) distributions, and the fluorine breakup probabilities $f[i,j]$ from the model, there is only one unknown Xe distribution for each hit-2 Xe^{q+} spectrum. For example, to model the hit-2 spectrum obtained by projecting F^{2+} from hit 1, the only unknown is the Xe^{q+} spectrum associated with the fluorine combination (F^{2+},F^{2+}). So by subtracting everything else from the spectrum, we obtain the unknown Xe distribution. Similarly we can obtain the Xe distributions associated with (F^{3+},F^{3+}) and (F^{4+},F^{4+}) from the projections of F^{3+} and F^{4+} onto hit 2. After those three distributions are known, we are down to one unknown Xe distribution, that associated with (F^{1+},F^{1+}). But, if we subtract all the known components from the hit-1 spectrum using our model, we are left with just that unknown Xe distribution. So this provides a way to proceed, and estimate all the breakup modes for XeF_2.

With our estimates of the Xe charge-state distributions for the various fluorine ion breakup modes, we have all the information needed to write down the final estimates for the XeF_2 breakup modes in coincidence with a $K\alpha$ photon, for photoionization of XeF_2 at the $1s^{-1}7\sigma_u$ resonance. The final results for the probabilities (in %) are given in Table IV along with the errors in the probabilities. The errors take into account statistical and systematic errors. The columns labeled F^{q2} and F^{q3} refer to the fluorine ion charge states, and the column labeled Xe^{q1} gives the xenon charge state for the particular mode. The sum over all the probabilities is 100%.

APPENDIX C: FLUORINE ION ENERGY CALCULATION FROM THE COULOMB MODEL

The experimental results for F^{q+} ion kinetic energies in Table II of the paper were determined from the splitting in the peak positions of the faster and slower components of each charge state [Fig. 2(b)]. This spectrum is averaged over all partner ions but modified by the detection efficiencies. The fluorine ion kinetic energies were related to the time required for a backward-directed ion to turn around and return to its starting position, assuming the symmetric mode in which the two fluorine ions had the same charge. A correction factor to account for the angular distribution of molecular axes selected by resonant excitation was also applied. Experimental uncertainties do not allow reliable kinetic energy estimates to be determined as a function of Xe charge state, so the results are an average over all Xe charge states. For each possible charge distribution channel (F^{q2},F^{q3},Xe^{q1}), the total potential energy $E_{\rm pot}$ of the molecular system was calculated using the equation

$$E_{\rm pot} = \frac{1}{4\pi\epsilon}\left[\frac{q_1q_2}{r_{12}} + \frac{q_1q_3}{r_{13}} + \frac{q_2q_3}{r_{23}}\right], \qquad \text{(C1)}$$

where $r_{12} = r_{13} = \frac{1}{2}r_{23} = 1.97$ Å, the ground-state Xe-F internuclear distance. In the limit that the Xe ion carries off no breakup kinetic energy, the two F ions break up with equal and opposite momentum and therefore equal energies, independent of their charge. The calculated energy per F ion is therefore one half the total potential energy. The calculated energies per F ion averaged over breakup modes were obtained using the deduced probabilities for each breakup channel from Table IV, taking the detection efficiencies into account. Results for the symmetric breakup modes are given in the third column of Table II. Column 4 presents the results averaged over all modes, in order to give an indication of the reliability of the symmetric-mode assumption.

APPENDIX D: SIMULATIONS OF THE ITOF SPECTROMETER; DISCUSSION OF THE F PEAK ASYMMETRIES IN FIG. 2(b)

Independent of the data analysis, simulations of the ITOF spectrometer used in the experiment (see Fig. 1) were carried out in an attempt to achieve a better understanding of our experimental conditions and observations. These involved ion

TABLE IV. The probability and errors (in %) for XeF_2 to break up into specific components(F^{q2}, F^{q3}, and Xe^{q1}), based on data from photoionization of XeF_2 with x rays tuned to the $1s^{-1}7\sigma_u$ molecular resonance.

F^{q2}	F^{q3}	Xe^{q1}	Probability (%)	Error
0	0	1	0.00	0.00
0	0	2	0.00	0.00
0	0	3	0.00	0.00
0	0	4	0.00	0.00
0	0	5	0.00	0.00
0	0	6	0.00	0.00
0	0	7	0.00	0.00
0	0	8	0.00	0.00
0	0	9	0.00	0.00
1	0	1	0.00	0.00
1	0	2	0.00	0.00
1	0	3	0.00	0.00
1	0	4	0.00	0.00
1	0	5	0.00	0.00
1	0	6	0.00	0.00
1	0	7	0.00	0.00
1	0	8	0.00	0.00
1	0	9	0.00	0.00
1	1	1	0.29	0.15
1	1	2	1.21	0.40
1	1	3	3.23	0.66
1	1	4	5.50	0.85
1	1	5	6.01	0.93
1	1	6	4.21	0.75
1	1	7	1.89	0.48
1	1	8	0.55	0.21
1	1	9	0.10	0.05
2	0	1	0.00	0.00
2	0	2	0.00	0.00
2	0	3	0.00	0.00
2	0	4	0.00	0.00
2	0	5	0.00	0.00
2	0	6	0.00	0.00
2	0	7	0.00	0.00
2	0	8	0.00	0.00
2	0	9	0.00	0.00
2	1	1	0.09	0.06
2	1	2	0.50	0.23
2	1	3	1.61	0.53
2	1	4	3.12	0.86
2	1	5	3.64	0.99
2	1	6	2.55	0.73
2	1	7	1.07	0.38
2	1	8	0.27	0.13
2	1	9	0.04	0.03
2	2	1	0.28	0.17
2	2	2	1.48	0.61
2	2	3	4.80	1.19
2	2	4	9.32	1.61
2	2	5	10.86	1.84
2	2	6	7.60	1.48
2	2	7	3.19	0.90
2	2	8	0.80	0.35
2	2	9	0.12	0.07
3	0	1	0.00	0.00

TABLE IV. (*Continued.*)

F^{q2}	F^{q3}	Xe^{q1}	Probability (%)	Error
3	0	2	0.00	0.00
3	0	3	0.00	0.00
3	0	4	0.00	0.00
3	0	5	0.00	0.00
3	0	6	0.00	0.00
3	0	7	0.00	0.00
3	0	8	0.00	0.00
3	0	9	0.00	0.00
3	1	1	0.01	0.01
3	1	2	0.06	0.04
3	1	3	0.34	0.15
3	1	4	1.05	0.32
3	1	5	1.79	0.47
3	1	6	1.68	0.46
3	1	7	0.88	0.28
3	1	8	0.25	0.11
3	1	9	0.04	0.03
3	2	1	0.01	0.01
3	2	2	0.10	0.06
3	2	3	0.55	0.21
3	2	4	1.68	0.34
3	2	5	2.87	0.41
3	2	6	2.70	0.42
3	2	7	1.41	0.31
3	2	8	0.41	0.15
3	2	9	0.07	0.04
3	3	1	0.00	0.00
3	3	2	0.02	0.02
3	3	3	0.21	0.13
3	3	4	1.07	0.39
3	3	5	2.45	0.62
3	3	6	2.45	0.64
3	3	7	1.07	0.37
3	3	8	0.21	0.11
3	3	9	0.02	0.01
4	0	1	0.00	0.00
4	0	2	0.00	0.00
4	0	3	0.00	0.00
4	0	4	0.00	0.00
4	0	5	0.00	0.00
4	0	6	0.00	0.00
4	0	7	0.00	0.00
4	0	8	0.00	0.00
4	0	9	0.00	0.00
4	1	1	0.00	0.00
4	1	2	0.00	0.00
4	1	3	0.03	0.02
4	1	4	0.07	0.06
4	1	5	0.12	0.09
4	1	6	0.11	0.08
4	1	7	0.05	0.04
4	1	8	0.01	0.01
4	1	9	0.00	0.00
4	2	1	0.00	0.00
4	2	2	0.01	0.01
4	2	3	0.06	0.03
4	2	4	0.18	0.09
4	2	5	0.32	0.15

TABLE IV. (*Continued.*)

F^{q2}	F^{q3}	Xe^{q1}	Probability (%)	Error
4	2	6	0.31	0.15
4	2	7	0.16	0.08
4	2	8	0.05	0.03
4	2	9	0.01	0.01
4	3	1	0.00	0.00
4	3	2	0.00	0.00
4	3	3	0.01	0.01
4	3	4	0.03	0.02
4	3	5	0.06	0.03
4	3	6	0.06	0.03
4	3	7	0.03	0.02
4	3	8	0.01	0.01
4	3	9	0.00	0.00
4	4	1	0.00	0.00
4	4	2	0.00	0.00
4	4	3	0.00	0.00
4	4	4	0.01	0.01
4	4	5	0.08	0.04
4	4	6	0.17	0.07
4	4	7	0.17	0.07
4	4	8	0.08	0.04
4	4	9	0.01	0.01

trajectory simulations using the software package SIMION [28]. The SIMION software allows the simulation of particle trajectories for given spectrometer geometry, electrode voltages, and mass, charge, and initial conditions of the ions. After fine-tuning such parameters as jet position, good agreement was found between the simulated and experimental ITOF data for Xe, and this geometry was used for subsequent simulations.

SIMION was used to help us understand the asymmetries in the intensities of the faster and slower F ion components in Fig. 2(b). Our fits show that the backward peaks are wider, thus the forward-backward asymmetries are less than the peak heights would imply. For example, for F^{2+}, the asymmetry in peak areas is ∼10% whereas the peak heights differ by ∼35%. One possibility was that the asymmetry was due to a difference in detection efficiency between the forward and backward ions. To explore this, SIMION calculations were carried out for F ions ejected with kinetic energies determined from the data. It was confirmed that ions ejected in both the forward and the backward directions subtend fairly small solid angles and reach the detector unobstructed by walls or apertures. These studies showed that it was unlikely that the asymmetry in F peaks was due to a difference in detection efficiency between fluorine ions with initial velocities toward the detector compared with fluorine ions with initial velocities away from the detector.

Having eliminated this as a possibility, we were able to confirm that the residual asymmetry is due to a rather large electronic dead time of ∼50 ns between successive hits in our experiment. In particular, for events in which the two F ions have the same charge, if the faster ion is detected, the dead time prevents detection of the slower ion.

[1] T. A. Carlson and R. M. White, J. Chem. Phys. **44**, 4510 (1966).
[2] E. Pomplun and G. Sutmann, Int. J. Radiat. Biol. **80**, 855 (2004).
[3] S. Corde, A. Joubert, J. F. Adam, A. M. Charvet, J. F. Le Bas, F. Estève, H. Elleaume, and J. Balosso, Br. J. Cancer **91**, 544 (2004).
[4] M. Mucke, M. Braune, S. Barth, M. Förstel, L. Lischke, V. Ulrich, T. Arion, U. Becker, A. Bradshaw, and U. Hergenhahn, Nat. Phys. **6**, 143 (2010).
[5] T. Jahnke, H. Sann, T. Havermeier, K. Kreidi, C. Stuck, M. Meckel, M. Schöffler, N. Neumann, R. Wallauer, S. Voss *et al.*, Nat. Phys. **6**, 139 (2010).
[6] B. Boudaïffa, P. Cloutier, D. Hunting, M. A. Huels, and L. Sanche, Science **287**, 1658 (2000).
[7] L. Caron, L. Sanche, S. Tonzani, and C. H. Greene, Phys. Rev. A **80**, 012705 (2009).
[8] T. M. Orlando, D. Oh, Y. Chen, and A. B. Aleksandrov, J. Chem. Phys. **128**, 195102 (2008).
[9] B. Esser, U. Ankerhold, N. Anders, and F. von Busch, J. Phys. B **30**, 1191 (1997).
[10] U. Ankerhold, B. Esser, and F. von Busch, J. Phys. B **30**, 1207 (1997).
[11] L. S. Cederbaum, J. Zobeley, and F. Tarantelli, Phys. Rev. Lett. **79**, 4778 (1997).
[12] J. Zobeley, L. S. Cederbaum, and F. Tarantelli, J. Phys. Chem. A **103**, 11145 (1999).
[13] R. Santra, J. Zobeley, L. S. Cederbaum, and N. Moiseyev, Phys. Rev. Lett. **85**, 4490 (2000).
[14] S. Marburger, O. Kugeler, U. Hergenhahn, and T. Möller, Phys. Rev. Lett. **90**, 203401 (2003).
[15] T. Jahnke, A. Czasch, M. Schöffler, S. Schössler, M. Käsz, J. Titze, K. Kreidi, R. E. Grisenti, A. Staudte, O. Jagutzki *et al.*, Phys. Rev. Lett. **99**, 153401 (2007).
[16] T. Jahnke, A. Czasch, M. S. Schöffler, S. Schössler, A. Knapp, M. Käsz, J. Titze, C. Wimmer, K. Kreidi, R. E. Grisenti *et al.* Phys. Rev. Lett. **93**, 163401 (2004).
[17] R. Santra and L. S. Cederbaum, Phys. Rev. Lett. **90**, 153401 (2003).
[18] Y. Morishita, X.-J. Liu, N. Saito, T. Lischke, M. Kato, G. Prümper, M. Oura, H. Yamaoka, Y. Tamenori, I. H. Suzuki *et al.*, Phys. Rev. Lett. **96**, 243402 (2006).
[19] C. Buth, R. Santra, and L. S. Cederbaum, J. Chem. Phys. **119**, 10575 (2003).
[20] G. B. Armen, E. P. Kanter, B. Krässig, J. C. Levin, S. H. Southworth, and L. Young, Phys. Rev. A **69**, 062710 (2004).
[21] E. M. Dufresne, B. Adams, D. A. Arms, M. Chollet, E. C. Landahl, Y. Li, D. A. Walko, and J. Wang, in *SRI 2009, Tenth International Conference on Synchrotron Radiation Instrumentation*, edited by R. Garrett, Ian Gentle, K. Nugent, and S. Wilkins, AIP Conf. Proc. No. 1234 (AIP, Melville, NY, 2010), p. 181.
[22] R. D. Deslattes, E. G. Kessler, P. Indelicato, L. de Billy, E. Lindroth, and J. Anton, Rev. Mod. Phys. **75**, 35 (2003).
[23] M. H. Chen, B. Crasemann, and H. Mark, Phys. Rev. A **21**, 436 (1980).

[24] H. Basch, J. W. Moskowitz, C. Hollister, and D. Hankin, J. Chem. Phys. **55**, 1922 (1971).
[25] S.-K. Son, L. Young, and R. Santra, Phys. Rev. A **83**, 033402 (2011).
[26] A. G. Kochur, A. I. Dudenko, V. L. Sukhorukov, and I. D. Petrov, J. Phys. B **27**, 1709 (1994).
[27] T. A. Carlson, W. E. Hunt, and M. O. Krause, Phys. Rev. **151**, 41 (1966).
[28] http://simion.com